Inorg. Chem. **2008**, *47*, 11583−11592

Computational Density Functional Study of Polypyrrolic Macrocycles: Analysis of Actinyl-Oxo to 3d Transition Metal Bonding

Joel J. Berard and Georg Schreckenbach*

Department of Chemistry, University of Manitoba, Winnipeg, Manitoba R3T 2N2, Canada

Polly L. Arnold, Dipti Patel, and Jason B. Love

School of Chemistry, University of Edinburgh, West Mains Road, Edinburgh EH9 3JJ, U.K.

Received June 11, 2008

Density functional theoretical methods are used to study heterobimetallic compounds of a new form of binucleating Schiff-base polypyrrolic macrocycle, denoted $[An^{VI}O_2(\mathbf{1})H_2L]$, $[An^{V}O_2(\mathbf{1})H_2L]^-$, $[An^{VI}O_2(\mathbf{TM})L]$ and $[An^{V}O_2(\mathbf{TM})L]^-$, and containing actinyl ions AnO_2^{n+} (An = U, Np, Pu; n = 1, 2) and 3d transition metals (TM): no TM = **1**, Mn = **2**, Fe = **3**, Co = **4**, and Zn = **5**. Calculated bond orders (TM−O2 = 0.36 to 0.81) provide evidence for partial bond formation between the transition metal (TM) and the actinyl-endo-oxygen for all 24 cases studied. Redox potentials for $[An^{VI}O_2(\mathbf{1})H_2L]/[An^{V}O_2(\mathbf{1})H_2L]^-$ couples were found to have the same $Np^{VI/V} > Pu^{VI/V} > U^{VI/V}$ trend as previously studied for the $[AnO_2(H_2O)_5]^{2+/1+}$ couples, where Np^{VI} is the most easily reduced to Np^{V}. Extrapolation from the earlier penta-aqua actinyl results is used to predict $[An^{VI}O_2(\mathbf{1})H_2L]/[An^{V}O_2(\mathbf{1})H_2L]^-$ redox couples of U = −1.10 eV, Np = 0.25 eV, and Pu = 0.01 eV. The calculated redox potential for $[U^{VI}O_2(\mathbf{1})H_2L]/[U^{V}O_2(\mathbf{1})H_2L]^-$ is within 0.08 eV of the value found by cyclic voltammetry (−1.18 eV, in THF/$NBu^n_4BF_4$ solvent).

Introduction

Transition metals, lanthanides, and actinides are increasingly used to demonstrate the multidentate chelating abilities of larger macrocyclic ligands such as crown ethers,[1,2] calixarenes,[1,3] expanded porphyrins,[1,4−9] and phthalocyanines.[1,9] Growing interest in complexing early actinides and their actinyls has been created because of the possibilities for the selective extraction of their radionuclides. The ability to vary ring size and to alter the identity of donor atoms has also resulted in the possibility for the tailoring of specific cations and oxidation states within the ligand cavities of such structures.

Recent experimental investigations[10−12] into polypyrrolic macrocycles[10,13−17] are reminiscent, structurally, of Pac-Man

* To whom correspondence should be addressed. E-mail: schrecke@cc.umanitoba.ca.

(1) Morss, L. R.; Edelstein, N. M.; Fuger, J. *The Chemistry of the Actinide and Transactinide Elements*, 3rd ed.; Springer: Dordrecht: The Netherlands, 2006.
(2) Bradshaw, J. S.; Izatt, R. M.; Bordunov, A. V.; Chu, C. Y.; Hathway, J. L. In *Comprehensive Supramolecular Chemistry: Molecular Recognition: Receptors for Cationic Guests*; Gokel, G. W., Ed.; Pergamon: Oxford, 1996; Vol. *1*, p 35.
(3) Thuery, P.; Nierlich, M.; Harrowfield, J. M.; Ogden, M. I., *Calixarenes*. Kluwer Academic: Dordrecht, The Netherlands, 2001; p 561.
(4) Sessler, J. L.; Camiolo, S.; Gale, P. A. *Coord. Chem. Rev.* **2003**, *240*, 17.
(5) Sessler, J. L.; Gorden, A. E. V.; Seidel, D.; Hannah, S.; Lynch, V.; Gordon, P. L.; Donohoe, R. J.; Tait, C. D.; Keogh, D. W. *Inorg. Chim. Acta* **2002**, *341*, 54.
(6) Sessler, J. L.; Seidel, D. *Angew. Chem., Int. Ed.* **2003**, *42*, 5134.
(7) Sessler, J. L.; Tomat, E.; Mody, T. D.; Lynch, V. M.; Veauthier, J. M.; Mirsaidov, U.; Markert, J. T. *Inorg. Chem.* **2005**, *44*, 2125.
(8) Sessler, J. L.; Vivian, A. E.; Seidel, D.; Burrell, A. K.; Hoehner, M.; Mody, T. D.; Gebauer, A.; Weghorn, S. J.; Lynch, V. *Coord. Chem. Rev.* **2001**, *216−217*, 411.
(9) Sessler, J. L.; Weghorn, S. J. *Tetrahedron Organic Chemistry Series: Expanded, Contracted and Isomeric Porphyrins*; Pergamon: Oxford, 1997; Vol. *15*.
(10) Arnold, P. L.; Patel, D.; Wilson, C.; Love, J. B. *Nature* **2008**, *451*, 315.
(11) Arnold, P. L.; Blake, A. J.; Wilson, C.; Love, J. B. *Inorg. Chem.* **2004**, *43*, 8206.
(12) Arnold, P. L.; Patel, D.; Blake, A. J.; Wilson, C.; Love, J. B. *J. Am. Chem. Soc.* **2006**, *128*, 9610.
(13) Givaja, G.; Blake, A. J.; Wilson, C.; Schroder, M.; Love, J. B. *Chem. Commun.* **2003**, 2508.
(14) Givaja, G.; Blake, A. J.; Wilson, C.; Schroder, M.; Love, J. B. *Chem. Commun.* **2005**, 4423.
(15) Givaja, G.; Volpe, M.; Edwards, M. A.; Blake, A. J.; Wilson, C.; Schroder, M.; Love, J. B. *Angew. Chem., Int. Ed.* **2007**, *46*, 584.
(16) Givaja, G. et al. *Chem.—Eur. J.* **2007**, *13*, 3707.
(17) Veauthier, J. M.; Tomat, E.; Lynch, V. M.; Sessler, J. L.; Mirsaidov, U.; Markert, J. T. *Inorg. Chem.* **2005**, *44*, 6736.

10.1021/ic8010772 CCC: $40.75
Published on Web 11/12/2008

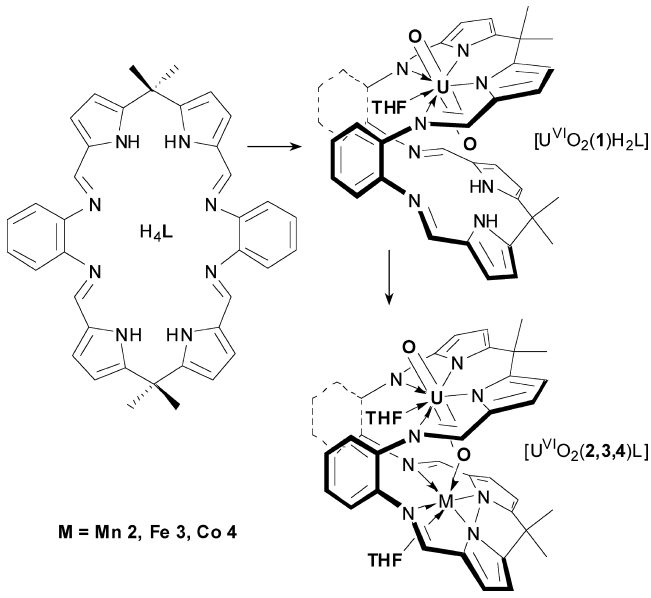

Figure 1. Synthesis of uranyl TM complexes $[U^{VI}O_2(\mathbf{1})H_2L]$ and $[U^{VI}O_2(\mathbf{2-4})L]$.[11,12] It is assumed that the complexes $[U^{VI}O_2(\mathbf{5})L]$ (M=Zn), $[An^{VI}O_2(\mathbf{1})H_2L]$, and $[An^{VI}O_2(\mathbf{2-5})L]$ and the singly reduced complexes $[An^{V}O_2(\mathbf{1})H_2L]^-$ and $[An^{V}O_2(\mathbf{2-5})L]$ have similar structures.

cofacial diporphyrins[18] that can accommodate a range of d- and f-block metals of various oxidation states. Such structures exhibit an abundance of chemical variation and are thought to offer potential chemical advantages. The binucleating Schiff-base calixpyrroles investigated possess the beneficial coordinative features of the pyrrole group along with the exceptional design characteristics and synthetic versatility of Schiff-base condensation procedures.

These experimental efforts[11,12] have shown that the transamination reaction between **H_4L** (Figure 1) and the uranyl bis(amide) $[UO_2(THF)_2\{N(SiMe_3)_2\}_2]$ in THF leads to the formation of a hinged complex which accommodates only one linear uranyl (UO_2^{2+}) $[U^{VI}O_2(\mathbf{1})H_2L]$ within one of the two available polypyrrolic cavities. The two aryl-groups of the polypyrrolic macrocycle function as hinges within a rigid molecular cleft-like structure in which the uranyl-endo-oxygen is hydrogen bonded to two adjacent pyrrolic hydrogens of the vacant N_4 cavity. A further transamination reaction with a transition metal amide $[M\{N(SiMe_3)_2\}_2]$ (M = Mn **2**, Fe **3**, and Co **4**) produces $[U^{VI}O_2(\mathbf{2-4})L]$, Figure 1. Crystals of $[U^{VI}O_2(\mathbf{1})H_2L]$, $[U^{VI}O_2(\mathbf{2})L]$, and $[U^{VI}O_2(\mathbf{4})L]$ were suitable for X-ray diffraction studies, whereas those of $[U^{VI}O_2(\mathbf{3})L]$ were found to be too weakly diffracting to yield useful structural information. The most striking discovery, identified for the first time within the isostructural bimetallic complexes $[U^{VI}O_2(\mathbf{2-4})L]$, was the interaction between the uranyl-endo-oxygen and the 3d transition metal (TM).

Such structures containing an interaction between the Lewis basic oxo-group of one cation with another metal cation are denoted "cation-cation" complexes. Actinyl cation−cation interactions are an uncommon but important feature in neptunyl[19] and plutonyl chemistry,[20] and are particularly rare in uranyl complexes.[21] Steele and Taylor recently elucidated the importance of actinyl cation−cation interactions, in a theoretical study of actinyl(V) disproportionation reactions, to spent nuclear fuel processing and environmental wastes.[22] Bimetallic complexes containing an actinide and a 3d TM are also relatively rare and are usually formed by using bridging ligands.[23−26] Complexes with two centers of reactivity offer the potential for variations and improvements in new and existing reaction chemistry and catalysis by TMs.

Our primary aim is to investigate the nature of bonding within these new complexes for the purpose of adding to the existing knowledge of these three classifications: polypyrrolic macrocycle, cation−cation, and bimetallic complexes. In particular, we are looking to exploit the actinyl-oxo group desymmetrization created by the bonding of the actinyl-endo-oxygen to the dicationic TMs: Mn^{II}, Fe^{II}, Co^{II}, and Zn^{II}. Access to the selective chemical reactivity of one of the actinyl oxygens would be a desirable addition to the understanding of the speciation of the early actinides found in the nuclear fuel cycle and radioactive wastes. Also, as a goal, we are looking to extend the experimentally known chemistry of the $U^{VI/V}$, $Np^{VI/V}$, and $Pu^{VI/V}$ series, Figure 1, through observations of periodic trends in structural variations, redox potentials, energetics, harmonic vibrations, and so forth. The redox chemistry of the early actinides is quite diverse because of the accessibility of higher oxidation states and the sensitivity of redox potentials to the metal's coordination environment.[27] Interest has been mostly driven by the need for developing separations and process chemistry relating to the nuclear fuel cycle. However, more recently the environmental concern of treating nuclear wastes containing this early series of actinide elements has led to increased interest.

Herein, we present the results of computational studies into the bond angles, bond lengths, bond orders, and atomic charges for 30 structures across both the actinyl (VI) and (V) and the TM series, Figure 1. Thus, in addition to the experimentally studied heterobimetallic complexes, this computational series also includes the transuranic (NpO_2^{n+}, and PuO_2^{n+}) heterobimetallic complexes $An^{VI}O_2(\mathbf{1-4})L]$ (An = Np, Pu), and the zinc analogues, $[An^{VI}O_2(\mathbf{5})L]$ and $[An^{V}O_2(\mathbf{5})L]^-$ (An = U, Np, Pu) in this work.

We have also calculated oxidation−reduction (redox) potentials for the set of complexes.[28]

(18) Chang, C. J.; Baker, E. A.; Pistorio, B. J.; Deng, Y. Q.; Loh, Z. H.; Miller, S. E.; Carpenter, S. D.; Nocera, D. G. *Inorg. Chem.* **2002**, *41*, 3102.

(19) Sullivan, J. C.; Hindman, J. C.; Zielen, A. J. *J. Am. Chem. Soc.* **1961**, *83*, 3373.

(20) Newton, T. W.; Burkhart, M. J. *Inorg. Chem.* **1971**, *10*, 2323.

(21) Newton, T. W.; Baker, F. B. *Inorg. Chem.* **1962**, *1*, 368.

(22) Steele, H.; Taylor, R. J. *Inorg. Chem.* **2007**, *46*, 6311.

(23) Cramer, R. E.; Higa, K. T.; Pruskin, S. L.; Gilje, J. W. *J. Am. Chem. Soc.* **1983**, *105*, 6749.

(24) Day, V. W.; Klemperer, W. G.; Maltbie, D. J. *Organometallics* **1985**, *4*, 104.

(25) Baudry, D.; Ephritikhine, M. *J. Organomet. Chem.* **1986**, *311*, 189.

(26) Kozimor, S. A.; Bartlett, B. M.; Rinehart, J. D.; Long, J. R. *J. Am. Chem. Soc.* **2007**, *129*, 10672.

(27) Morris, D. E. *Inorg. Chem.* **2002**, *41*, 3542.

(28) Li, J.; Fisher, C. L.; Chen, J. L.; Bashford, D.; Noodleman, L. *Inorg. Chem.* **1996**, *35*, 4694.

Methods of Calculation

Since the largest structures studied contain 108 atoms including a heavy actinide element, the calculation requirements limit us to the use of only a few theoretical and computational methods that allow for the completion of calculations in a reasonable amount of time.[29]

With the inclusion of electron correlation, density functional theory (DFT)[30−32] is known to have definite advantages for TMs and actinides while often offering a significant time saving advantage over comparable ab initio methods. (We note, however, that approximate DFT is, of course, no panacea, see also below.) Gradient corrected calculations with the PBE[33] exchange-correlation (XC) functional offer additional time savings over the popular B3LYP[34−36] hybrid functional; while on average providing slightly less accurate Gibbs free energies,[37] the PBE functional is often found to provide as accurate geometries and vibrational frequencies. Furthermore, additional time is saved with the incorporation of resolution-of-identity (RI)[38] approximation methods, where an auxiliary basis set is used to improve the computational efficiency of the Priroda code.[38−42] Recent development of accurate relativistic methods has also played a significant part in the ability to model such structures accurately. Our research group has been able to verify the accuracy of three separate relativistic methods for a variety of actinide containing complexes:[37,43−45] the all-electron (AE) scalar four-component method (Priroda), the ZORA (zero order regular approximation)[46−49] method (ADF),[50] and the Stuttgart-Dresden SC-ECP (small-core effective core potential) method of Küchle et al.[51] (Gaussian). Lastly, the incorporation of Hay spin−orbit coupling and multiplet ad hoc corrections[52] have been determined to be necessary to obtained accurate oxidation−reduction potentials in solution. As for solvation methods we have gained confidence in using both the ADF-COSMO (conductor-like screening model)[53−55] and the Gaussian C-PCM (conductor polarized continuum model)[56] to calculate single-point energies. The remainder of this section outlines the methods used in this work.

Unconstrained gas-phase geometry optimizations were performed using version 5 of the Priroda program (p5).[38−42] The Priroda code employs a fast RI method for calculating both Coulomb and exchange-correlation (XC) integrals with optimized fitted Gaussian basis sets. For relativistic effects in p5 an AE scalar four-component process was applied where all spin−orbit terms are separated out from the scalar terms[41,57] and neglected.[38−42] Calculations with p5 were performed using the gradient corrected PBE XC functional and the correlation consistent polarized valence triple-ζ (cc-pVTZ)[41] Gaussian basis set for the large component, and the corresponding kinetically balanced basis for the small component. Harmonic vibrational frequencies were calculated to obtain thermochemistry data, such as Gibbs free energies and zero-point energy corrections, and also to verify the nature of stationary points on the potential energy surface (i.e., of the optimized geometries).

Systems with unpaired electrons used an unrestricted, open-shell Kohn−Sham formalism. The multiplicities ($2S + 1$) were determined based on TMs with weak field/high spin tetrahedral coordination of crystal field theory. Four categories of orbital occupations are found to occur for the bimetallic complexes being investigated: (1) where no unpaired electrons are found on either metal in the $[U^{VI}O_2(\mathbf{1})H_2L]$ and $[U^{VI}O_2(\mathbf{5})L]$ complexes, (2) where unpaired electrons are found only on the actinide metal in the $[U^{V}O_2(\mathbf{1})H_2L]^-$ and $[U^{V}O_2(\mathbf{5})L]^-$, $[Np^{VI}O_2(\mathbf{1})H_2L]$ and $[Np^{VI}O_2(\mathbf{5})L]$, $[Np^{V}O_2(\mathbf{1})H_2L]^-$ and $[Np^{V}O_2(\mathbf{5})L]^-$, $[Pu^{VI}O_2(\mathbf{1})H_2L]$ and $[Pu^{VI}O_2(\mathbf{5})L]$, and $[Pu^{V}O_2(\mathbf{1})H_2L]^-$ and $[Pu^{V}O_2(\mathbf{5})L]^-$ complexes, (3) where unpaired electrons are found only on the TM in the $[U^{VI}O_2(\mathbf{2}\text{-}\mathbf{4})L]$ complexes, and (4) where unpaired electrons are found on both metals at the same time in the remaining TM complexes. In such cases, placement of the unpaired electrons within the chosen weak field tetrahedral crystal field environment, were taken to be always parallel to each other (high spin), because of the difficulties of implementing anti-parallel configurations with the software used. Efforts were made within p5 and ADF to model the distinguishing electron arrangements of these four categories of orbital occupations.

Several previous internal efforts have been made toward establishing the performance of the relativistic AE-DFT calculations with the Priroda code as applied to the simulation of actinide and actinyl molecules. Various test calculations were performed on small molecules such as actinyl cations, actinide fluorides, oxides, and oxofluorides,[37] as well as larger molecules such as dinitrogen tetroxide adducts of uranyl nitrate,[58] actinyl aquo complexes,[43,44] and complexes between actinides and various macrocycles.[45,59,60] In all such cases Priroda was determined to be an expedient and

(29) Schreckenbach, G.; Hay, P. J.; Martin, R. L. *J. Comput. Chem.* **1999**, *20*, 70.
(30) Cramer, C. J. *Essentials of Computational Chemistry: Theories and Models*, 2nd ed.; Wiley: New York, 2004.
(31) Koch, W.; Holthausen, M. C. *A Chemist's Guide to Density Functional Theory*; Verlag Chemie: New York, 2000.
(32) Tsipis, C. A. *Comments Inorg. Chem.* **2004**, *25*, 19.
(33) Perdew, J. P.; Burke, K.; Ernzerhof, M. *Phys. Rev. Lett.* **1996**, *77*, 3865.
(34) Becke, A. D. *J. Chem. Phys.* **1993**, *98*, 5648.
(35) Lee, C.; Yang, W.; Parr, R. G. *Phys. Rev. B: Condens. Matter* **1988**, *37*, 785.
(36) Stephens, P. J.; Devlin, F. J.; Chabalowski, C. F.; Frisch, M. J. *J. Phys. Chem.* **1994**, *98*, 11623.
(37) Shamov, G. A.; Schreckenbach, G.; Vo, T. *Chem.—Eur. J.* **2007**, *13*, 4932.
(38) Laikov, D. N. *Chem. Phys. Lett.* **1997**, *281*, 151.
(39) Laikov, D. N. In *An implementation of the scalar relativistic density functional theory for molecular calculations with Gaussian basis sets*, poster presentation, DFT2000 Conference: Menton, France, June 2000.
(40) Laikov, D. N. Ph.D. Thesis, Moscow State University, 2000.
(41) Laikov, D. N. *Chem. Phys. Lett.* **2005**, *416*, 116.
(42) Laikov, D. N.; Ustynyuk, Y. A. *Russ. Chem. Bull.* **2005**, *54*, 820.
(43) Shamov, G. A.; Schreckenbach, G. *J. Phys. Chem. A* **2005**, *109*, 10961.
(44) Shamov, G. A.; Schreckenbach, G. *J. Phys. Chem. A* **2006**, *110*, 12072.
(45) Shamov, G. A.; Schreckenbach, G.; Martin, R. L.; Hay, P. J. *Inorg. Chem.* **2008**, *47*, 1465.
(46) van Lenthe, E.; Baerends, E. J.; Snijders, J. G. *J. Chem. Phys.* **1993**, *99*, 4597.
(47) van Lenthe, E.; Baerends, E. J.; Snijders, J. G. *J. Chem. Phys.* **1994**, *101*, 9783.
(48) van Lenthe, E.; Ehlers, A.; Baerends, E. J. *J. Chem. Phys.* **1999**, *110*, 8943.
(49) van Lenthe, E.; van Leeuwen, R.; Baerends, E. J. *Int. J. Quantum Chem.* **1996**, *57*, 281.
(50) Baerends, E. J. et al. *ADF 2006.01*; Scientific Computing and Modelling, Theoretical Chemistry, Vrije Universiteit: Amsterdam, The Netherlands, 2006.
(51) Küchle, W.; Dolg, M.; Stoll, H.; Preuss, H. *J. Chem. Phys.* **1994**, *100*, 7535.
(52) Hay, P. J.; Martin, R. L.; Schreckenbach, G. *J. Phys. Chem. A* **2000**, *104*, 6259.
(53) Pye, C. C.; Ziegler, T. *Theor. Chem. Acc.* **1999**, *101*, 396.
(54) Klamt, A.; Jonas, V.; Bürger, T.; Lohrenz, J. C. W. *J. Phys. Chem. A* **1998**, *102*, 5074.
(55) Klamt, A.; Schüürmann, G. *J. Chem. Soc., Perkin Trans. 2* **1993**, *2*, 799.
(56) Cossi, M.; Rega, N.; Giovanni, S.; Barone, V. *J. Comput. Chem.* **2003**, *24*, 669.
(57) Dyall, K. G. *J. Chem. Phys.* **1994**, *100*, 2118.
(58) Berard, J. J.; Shamov, G. A.; Schreckenbach, G. *J. Phys. Chem. A* **2007**, *101*, 10789.
(59) Shamov, G. A.; Schreckenbach, G. *J. Phys. Chem. A* **2006**, *110*, 9486.
(60) Shamov, G. A.; Schreckenbach, G. *Inorg. Chem.* **2008**, *47*, 805.

reliable code providing essentially the same results as other relativistic methods, provided the same XC functionals and reasonably converged basis sets are used.

Mulliken population density[61] based Mayer bond orders[62,63] were calculated with p5 using the PBE XC functional. Atomic charges were also determined within p5 with PBE using a method developed by Hirshfeld.[64] Both bond orders and atomic charges are not quantum mechanical observables but have been found to be useful in describing the chemical environment for a variety of actinide and actinyl complexes.[37,43−45,58,59]

Reduction potentials for ferrocenium/ferrocene and the actinyl VI/V series of complexes[43,52,59,65] required the calculation of free energies of solvation with the ADF-COSMO[53−55] model using THF as the solvent with a dielectric constant of 7.58. The current version of Priroda does not contain continuum solvation models. ADF-COSMO single-point calculations, with an integration parameter of 5.5, were therefore performed on the p5-optimized geometries with the same relativistic method, basis set, XC functional and conditions as described above (ADF ZORA/PBE/TZP/COSMO). Klamt radii were used for the main group atoms (O = 1.72 Å, N = 1.83 Å, C = 2.00 Å, and H = 1.30 Å).[54] Radii of 1.50 Å for all TMs and 1.70 Å for all An's were also used.[59] Although there is in fact some variation in the radii along each of the metal series, it is thought that with each of the metals being either coordinated or sterically hindered on all sides within the two cavities that the variation in radii across each of the metal series would have minimal effect on calculations in solution.

The reduction of the $[An^{VI}O_2(\mathbf{1})H_2L]$ complexes leads to the anionic pentavalent $[An^{V}O_2(\mathbf{1})H_2L]^-$ complexes described in the following redox half-reaction (reaction 1). The complementary ferrocenium/ferrocene half-reaction is then used to balance the electron transfer reaction (reaction 2).

$$[An^{VI}O_2(\mathbf{1})H_2L] + e^- \rightarrow [An^{V}O_2(\mathbf{1})H_2L]^- \quad (1)$$

$$Cp_2Fe^+ + e^- \rightarrow Cp_2Fe \quad (2)$$

The inclusion of "Hay corrections", based on model spin−orbit CI calculations,[52] is found to be necessary. The corrections account for multiplet and spin−orbit effects not included in a single-configuration DFT wave function. Corrections of −0.31, −1.17, and −0.21 eV were applied for U, Np, and Pu.

The use of DFT for the calculation of actinyl redox potentials has been discussed in detail in the literature.[43,52,66] In particular, Tsushima[66] notes a considerable difference in calculated uranium (VI)/(V) and ferrocene/ferrocenium redox potentials between DFT (B3LYP), CASPT2, and CCSD(T) with the latter performing best for uranium, and CASPT2 for the iron case. In a related study, Vallet et al.[67] studied the reduction of uranyl by hydrogen using again B3LYP, CASPT2, and CCSD(T). These studies show similarly large differences between the DFT and the correlated ab initio methods.

(61) Mulliken, R. S. *J. Chem. Phys.* **1955**, *23*, 1833.
(62) Bridgeman, A. J.; Cavigliasso, G.; Ireland, L. R.; Rothery, J. *J. Chem. Soc., Dalton Trans.* **2001**, 2095.
(63) Mayer, I. *Chem. Phys. Lett.* **1983**, *97*, 270.
(64) Hirshfeld, F. L. *Theor. Chim. Acta* **1977**, *44*, 129.
(65) Jaque, P.; Marenich, A. V.; Cramer, C. J.; Truhlar, D. G. *J. Phys. Chem. C* **2007**, *111*, 5783.
(66) Tsushima, S.; Wahlgren, U.; Grenthe, I. *J. Phys. Chem. A* **2006**, *110*, 9175.
(67) Vallet, V.; Schimmelpfennig, B.; Maron, L.; Teichteil, C.; Leininger, T.; Gropen, O.; Grenthe, I.; Wahlgren, U. *Chem. Phys.* **1999**, *244*, 185.

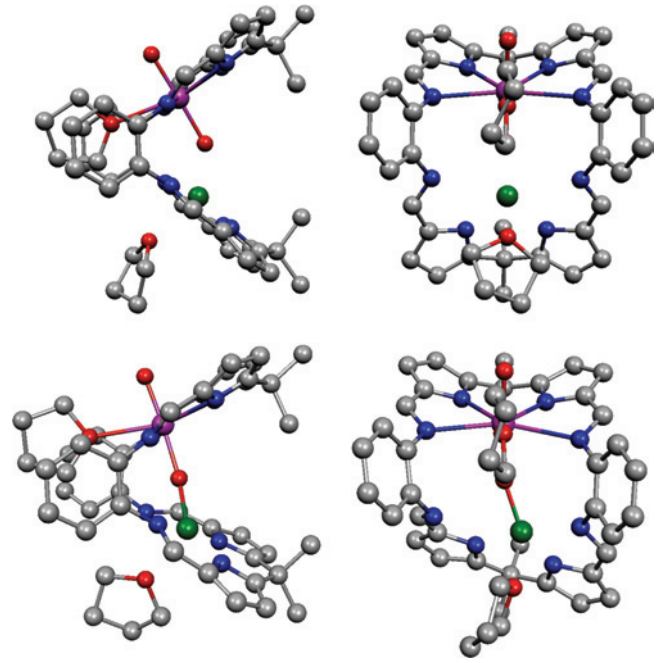

Figure 2. Optimized complexes of case 1, e.g. $[Pu^{V}O_2(\mathbf{2})L]^-$, (top views) and case 2, e.g. $[Pu^{VI}O_2(\mathbf{2})L]$, (bottom views) (magenta, Pu; green, Mn^{II}; red, O; blue, N; gray, C; and H excluded). The various other case 1 and 2 complexes have similar optimized structures, see the text.

Results and Discussion

A. Structure. (i) Metal Coordination Environments. All 30 structures contain actinides that consistently form 7-coordinate, near-pentagonal bipyramids with the actinide metal centrally located within a cavity plane formed by the four ring nitrogens (see, e.g., top front right-hand side view of $[Pu^{V}O_2(\mathbf{2})L]^-$ complex, Figure 2). The other coordination sites are filled by the two axial actinyl oxygens and the oxygen of an equatorial coordinating THF solvent molecule.

The predominant structural formation of the second cavity, case 1, is a 4-coordinate TM and is found to account for 16 of the 24 TM complexes. The strong coordination of the two pyrrolic nitrogens and intermediate coordination to both the oxygen of a THF solvent molecule and the actinyl-endo oxygen form a near tetrahedral coordination environment, whereas, the two Schiff-base nitrogens are considered to have minimal bonding interactions at distances of ≥2.599 Å from the TM centers ($[Pu^{V}O_2(\mathbf{2})L]^-$ complex, top views, Figure 2).

The O2−M−O4 bond angle of the case 1 TM structures provides us with a measure of the near tetrahedral formation created between the two oxygens and two pyrrolic nitrogens within these complexes, Table 1. The O2−M−O4 bond angle is seen to range from 122.5 to 140.1° compared to 109.5° for purely tetrahedral formations.

The remaining eight TM complexes make up two other structural cases. Case 2, has a much stronger bonding to one of the Schiff-base nitrogens. The additional bond to nitrogen leads to three 5-coordinate TM structures: $[Np^{VI}O_2(\mathbf{2})L]$, $[Pu^{VI}O_2(\mathbf{2})L]$, and $[Pu^{VI}O_2(\mathbf{3})L]$ (bottom views of Figure 2). Whereas, case 3 has no TM-THF bond and is seen in the following five complexes: $[U^{V}O_2(\mathbf{3})L]^-$, $[Np^{V}O_2(\mathbf{3})L]^-$,

Table 1. Gas-Phase Bond Angles for $[An^{VI}O_2(\mathbf{1})H_2L]$, $[An^{V}O_2(\mathbf{1})H_2L]^-$, $[An^{VI}O_2(\mathbf{2}\text{-}\mathbf{5})L]$, and $[An^{V}O_2(\mathbf{2}\text{-}\mathbf{5})L]^-$ Complexes (degree)[a]

complexes	O1−An−O2	N1−An−O3	N1,3−An−N2,4	N2−An−N3	An−O2−M	O2−M−O4	cofacial angle[e]
$[U^{VI}O_2(\mathbf{1})H_2L]$	175.3	77.3	67.0(0)	70.3			57.0(1)
exptl.[b]	177.6	76.6	66.8(1)	71.1			
$[U^{V}O_2(\mathbf{1})H_2L]^-$	175.7	78.3	65.4(1)	70.3			56.3(1)
$[Np^{VI}O_2(\mathbf{1})H_2L]$	178.1	76.5	67.3(1)	71.2			56.7(0)
$[Np^{V}O_2(\mathbf{1})H_2L]^-$	176.5	78.2	65.1(0)	70.3			56.2(1)
$[Pu^{VI}O_2(\mathbf{1})H_2L]$	179.2	77.9	66.2(1)	69.9			56.3(1)
$[Pu^{V}O_2(\mathbf{1})H_2L]^-$	177.2	78.6	65.2(0)	70.0			56.1(1)
$[U^{VI}O_2(\mathbf{2})L]$	175.9	76.9	67.8(2)	70.9	147.5	137.6	60.9(2)
exptl.[b]	177.4	76.7	68.5(6)	71.6			
$[U^{V}O_2(\mathbf{2})L]^-$	176.4	78.0	66.5(1)	71.5	144.1	137.1	62.9(1)
$[Np^{VI}O_2(\mathbf{2})L]$[c]	177.4	76.8	67.7(4)	71.6	147.1	139.5	59.4(9)
$[Np^{V}O_2(\mathbf{2})L]^-$	176.8	77.9	66.8(1)	71.5	144.7	137.5	62.0(1)
$[Pu^{VI}O_2(\mathbf{2})L]$[c]	175.6	78.7	66.6(4)	71.2	161.6	124.9	56.3(43)
$[Pu^{V}O_2(\mathbf{2})L]^-$	178.1	78.3	66.7(1)	70.8	142.4	139.1	62.3(1)
$[U^{VI}O_2(\mathbf{3})L]$	178.0	76.8	67.6(2)	71.1	144.9	140.1	59.3(2)
$[U^{V}O_2(\mathbf{3})L]^-$[d]	175.7	78.2	66.4(0)	70.1	143.7	none	64.5(1)
$[Np^{VI}O_2(\mathbf{3})L]$	179.3	76.6	67.6(3)	71.4	145.6	140.1	58.8(1)
$[Np^{V}O_2(\mathbf{3})L]^-$[d]	178.3	77.7	66.7(0)	70.9	142.7	none	63.6(2)
$[Pu^{VI}O_2(\mathbf{3})L]$[c]	176.7	77.8	67.1(5)	71.3	151.5	136.3	57.8(30)
$[Pu^{V}O_2(\mathbf{3})L]^-$[d]	179.5	77.9	66.6(1)	70.5	141.3	none	63.7(1)
$[U^{VI}O_2(\mathbf{4})L]$	175.0	76.9	67.6(2)	70.8	153.4	132.2	58.5(0)
exptl.[b]	177.8	76.3	67.3(3)	71.6			
$[U^{V}O_2(\mathbf{4})L]^-$	175.8	78.0	66.2(1)	71.2	148.5	133.1	60.1(1)
$[Np^{VI}O_2(\mathbf{4})L]$	178.4	76.3	67.6(1)	71.4	150.9	133.6	58.1(0)
$[Np^{V}O_2(\mathbf{4})L]^-$	176.8	77.9	66.4(1)	70.9	147.0	134.1	60.1(2)
$[Pu^{VI}O_2(\mathbf{4})L]$	178.8	77.9	66.8(1)	69.7	148.2	134.9	59.1(1)
$[Pu^{V}O_2(\mathbf{4})L]^-$	178.0	78.2	66.4(1)	70.5	145.7	135.2	59.8(1)
$[U^{VI}O_2(\mathbf{5})L]$	174.4	77.0	67.6(1)	70.6	159.5	122.5	59.0(0)
$[U^{V}O_2(\mathbf{5})L]^-$[d]	175.4	78.3	66.3(1)	70.1	147.4	none	63.9(1)
$[Np^{VI}O_2(\mathbf{5})L]$	178.0	76.4	67.6(1)	71.4	156.1	124.3	58.8(1)
$[Np^{V}O_2(\mathbf{5})L]^-$[d]	178.7	77.6	66.5(1)	70.7	144.8	none	63.4(1)
$[Pu^{VI}O_2(\mathbf{5})L]$	178.6	78.1	66.8(1)	69.7	153.2	125.5	59.9(0)
$[Pu^{V}O_2(\mathbf{5})L]^-$	178.2	78.2	66.4(1)	70.5	150.4	127.1	61.0(0)

[a] O1 exo, O2 endo, O3 An THF, O4 M THF, M = Mn **2**, Fe **3**, Co **4**, and Zn **5**. [b] For preceding complex, reference 12. [c] case 2 (3 short M−N bonds). [d] case 3 (no M−O4 bond). [e] Brackets contain maximum deviation from average, see text for definition.

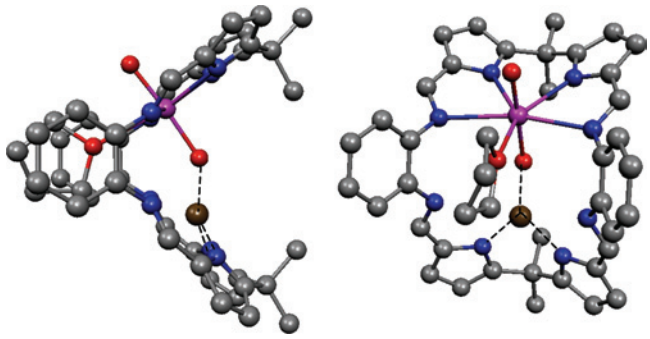

Figure 3. Optimized case 3 complex of $[U^{V}O_2(\mathbf{3})L]^-$ (side and front view, brown Fe^{II}).

$[Pu^{V}O_2(\mathbf{3})L]^-$, $[U^{V}O_2(\mathbf{5})L]^-$, and $[Np^{V}O_2(\mathbf{5})L]^-$ (Figure 3). In this situation, the loss of the THF bond results in 3-coordinate TM structures.

(ii) Bond Angles, Bond Lengths, Bond Orders, and Atomic Charges. Although the nature of An=O orbital bonding in early actinide complexes is considered to be quite complicated, the same linear structure is seen for both AnO_2^{2+} and AnO_2^{+} but with longer metal−oxygen bonds found in AnO_2^{+} because of the reduced charge on the metal (Table 2). A decrease in the strength accompanied by a shorter An=O bond is seen along the actinide series with increasing atomic number. One might have expected, that with the shorter An=O bond length created by the increase in the density of nuclear charge across the An series, a stronger bond would have formed but a weakening of the bond occurs because of the "actinide contraction" of the 5f orbitals.[68]

In general, bonding to the early actinides is best viewed as being intermediate between the strongly ionic bonding for lanthanides and the more covalent bonding for d-block transition elements. For the most part actinyl-ligand bonds in the equatorial or nearly in the equatorial plane are determined by a combination of the electrostatic attraction to the actinide, electrostatic repulsions between ligands, and steric demands around the metal center. Such bonds are usually described as predominantly ionic in nature and are often relatively weak and kinetically labile in solution.[1]

The structural data gathered from X-ray diffraction measurements for three of the uranyl complexes were used to gauge the accuracy of the gas-phase calculations in reproducing the solid-state experimental geometries. For the $[U^{VI}O_2(\mathbf{1})H_2L]$ structure, the five bond angles measured had a mean deviation between theory and experiment of 0.9°, with the largest deviation of 2.3° found for the O=U=O angle (Table 1). Whereas, for the seven bond lengths compared with experiment, a mean deviation of 0.030 Å was obtained (Table 2). This is considered to be a reasonably good result, and in line with previous results obtained for other polypyrrolic macrocyclic ligands.[59]

As for the larger $[U^{VI}O_2(\mathbf{2})L]$ and $[U^{VI}O_2(\mathbf{4})L]$ structures (108 atoms) the mean angle deviations were found to be 0.8° and 0.9°, respectively (Table 1). The total mean deviations of the fourteen bonds measured were determined to be 0.066

Table 2. Gas-Phase Bond Lengths for $[An^{VI}O_2(\mathbf{1})H_2L]$ and $[An^{V}O_2(\mathbf{1})H_2L]^-$ Complexes (Å)[a]

complex	An=O1	An=O2	An−O3	An−N1,4[c]	An−N2,3
$[U^{VI}O_2(\mathbf{1})H_2L]$	1.799	1.835	2.484	2.609(1)	2.466(1)
exptl.[b]	1.766	1.790	2.442	2.586(8)	2.443(1)
$[U^{V}O_2(\mathbf{1})H_2L]^-$	1.825	1.886	2.553	2.702(2)	2.531(1)
$[Np^{VI}O_2(\mathbf{1})H_2L]$	1.783	1.817	2.468	2.615(0)	2.452(0)
$[Np^{V}O_2(\mathbf{1})H_2L]^-$	1.817	1.890	2.586	2.723(3)	2.540(0)
$[Pu^{VI}O_2(\mathbf{1})H_2L]$	1.784	1.821	2.505	2.643(4)	2.490(1)
$[Pu^{V}O_2(\mathbf{1})H_2L]^-$	1.807	1.870	2.579	2.719(2)	2.535(0)

[a] O1 exo, O2 endo, O3 An THF. [b] For preceding complex, reference 12. [c] Brackets contain maximum deviation from average.

Table 3. Gas-Phase Mayer Bond Orders[63,70] for $[An^{VI}O_2(\mathbf{1})H_2L]$ and $[An^{V}O_2(\mathbf{1})H_2L]^-$ Complexes[a]

complex	An=O1	An=O2	An−O3	An−N1,4[b]	An−N2,3
$[U^{VI}O_2(\mathbf{1})H_2L]$	2.42	2.20	0.41	0.42(1)	0.57(0)
$[U^{V}O_2(\mathbf{1})H_2L]^-$	2.42	2.05	0.32	0.31(1)	0.47(0)
$[Np^{VI}O_2(\mathbf{1})H_2L]$	2.40	2.20	0.41	0.40(1)	0.55(0)
$[Np^{V}O_2(\mathbf{1})H_2L]^-$	2.41	1.99	0.28	0.29(0)	0.45(0)
$[Pu^{VI}O_2(\mathbf{1})H_2L]$	2.38	2.15	0.36	0.38(1)	0.48(1)
$[Pu^{V}O_2(\mathbf{1})H_2L]^-$	2.39	2.01	0.28	0.28(0)	0.44(0)

[a] O1 exo, O2 endo, O3 An THF. [b] Brackets contain maximum deviation from average.

Table 4. Gas-Phase Bond Lengths for $[An^{VI}O_2(\mathbf{2\text{-}5})L]$ and $[An^{V}O_2(\mathbf{2\text{-}5})L]^-$ Complexes (Å)[a]

complex	An=O1	An=O2	An−O3	An−N1,4[e]	An−N2,3	An−M	M−O2	M−O4	M−N5	M−N6,7	M−N8
$[U^{VI}O_2(\mathbf{2})L]$	1.805	1.860	2.535	2.538(4)	2.447(2)	3.770	2.066	2.303	2.599	2.073(10)	2.909
exptl.[b]	1.768	1.808	2.458	2.498(10)	2.426(9)	3.804	2.163	2.216	2.547	2.127(7)	2.659
$[U^{V}O_2(\mathbf{2})L]^-$	1.836	1.931	2.600	2.633(4)	2.498(1)	3.701	1.959	2.466	2.797	2.096(5)	2.937
$[Np^{VI}O_2(\mathbf{2})L]$[c]	1.800	1.889	2.581	2.555(2)	2.447(6)	3.712	1.982	2.329	2.293	2.032(14)	3.049
$[Np^{V}O_2(\mathbf{2})L]^-$	1.825	1.911	2.621	2.623(5)	2.486(1)	3.694	1.965	2.443	2.762	2.099(6)	2.917
$[Pu^{VI}O_2(\mathbf{2})L]$[c]	1.808	1.960	2.589	2.575(10)	2.473(3)	3.745	1.834	2.282	2.133	1.962(9)	3.297
$[Pu^{V}O_2(\mathbf{2})L]^-$	1.815	1.904	2.618	2.618(5)	2.492(1)	3.656	1.958	2.431	2.741	2.095(6)	2.906
$[U^{VI}O_2(\mathbf{3})L]$	1.806	1.890	2.545	2.553(4)	2.450(1)	3.679	1.969	2.227	2.888	2.003(4)	2.720
$[U^{V}O_2(\mathbf{3})L]^-$[d]	1.842	1.972	2.640	2.620(2)	2.498(1)	3.639	1.858	none	2.997	2.007(2)	3.039
$[Np^{VI}O_2(\mathbf{3})L]$	1.793	1.878	2.538	2.548(3)	2.444(4)	3.670	1.964	2.213	2.670	2.003(7)	2.901
$[Np^{V}O_2(\mathbf{3})L]^-$[d]	1.820	1.945	2.621	2.620(6)	2.488(0)	3.605	1.861	none	2.947	2.009(4)	3.041
$[Pu^{VI}O_2(\mathbf{3})L]$[c]	1.807	1.973	2.649	2.561(11)	2.465(3)	3.677	1.821	2.268	2.111	1.918(13)	3.212
$[Pu^{V}O_2(\mathbf{3})L]^-$[d]	1.811	1.934	2.623	2.611(3)	2.490(1)	3.576	1.856	none	2.939	2.006(3)	3.007
$[U^{VI}O_2(\mathbf{4})L]$	1.803	1.859	2.516	2.540(5)	2.450(2)	3.751	1.995	2.150	2.790	1.969(3)	2.930
exptl.[b]	1.772	1.783	2.474	2.525(12)	2.412(10)	3.726	2.086	2.117	2.445	1.988(15)	3.006
$[U^{V}O_2(\mathbf{4})L]^-$	1.835	1.935	2.593	2.636(5)	2.505(1)	3.697	1.907	2.234	2.914	1.982(2)	2.997
$[Np^{VI}O_2(\mathbf{4})L]$	1.789	1.847	2.508	2.542(6)	2.444(2)	3.715	1.991	2.152	2.775	1.970(4)	2.927
$[Np^{V}O_2(\mathbf{4})L]^-$	1.822	1.916	2.612	2.629(4)	2.502(2)	3.673	1.915	2.224	2.911	1.981(0)	2.959
$[Pu^{VI}O_2(\mathbf{4})L]$	1.788	1.854	2.535	2.545(8)	2.490(1)	3.676	1.968	2.154	2.752	1.971(7)	2.946
$[Pu^{V}O_2(\mathbf{4})L]^-$	1.812	1.903	2.610	2.621(5)	2.500(1)	3.650	1.916	2.220	2.871	1.981(2)	2.960
$[U^{VI}O_2(\mathbf{5})L]$	1.802	1.858	2.499	2.545(4)	2.450(1)	3.814	2.018	2.244	2.921	1.964(3)	3.025
$[U^{V}O_2(\mathbf{5})L]^-$[d]	1.842	1.958	2.628	2.636(1)	2.503(1)	3.675	1.871	none	3.140	1.967(2)	3.152
$[Np^{VI}O_2(\mathbf{5})L]$	1.787	1.844	2.493	2.549(5)	2.443(1)	3.783	2.022	2.247	2.903	1.967(3)	3.019
$[Np^{V}O_2(\mathbf{5})L]^-$[d]	1.817	1.931	2.611	2.636(1)	2.496(2)	3.631	1.879	none	3.133	1.967(1)	3.129
$[Pu^{VI}O_2(\mathbf{5})L]$	1.786	1.848	2.518	2.575(26)	2.491(0)	3.749	2.006	2.252	2.898	1.965(0)	3.022
$[Pu^{V}O_2(\mathbf{5})L]^-$	1.809	1.896	2.591	2.628(5)	2.499(1)	3.700	1.930	2.460	2.980	1.980(2)	3.051

[a] O1 exo, O2 endo, O3 An THF, O4 M THF, M = Mn **2**, Fe **3**, Co **4**, Zn **5**. [b] For preceding complex, reference 12. [c] Case 2 (3 short M−N bonds). [d] Case 3 (no M−O4 bond). [e] Brackets contain maximum deviation from average.

Å and 0.062 Å (Table 4). The larger than expected non-systematic deviations can be attributed to the Mn−N8 bond distance with a deviation of 0.250 Å in the $[U^{VI}O_2(\mathbf{2})L]$ complex and the Co−N5 bond distance with a deviation of 0.345 Å in the $[U^{VI}O_2(\mathbf{4})L]$ complex. If these two poor results are neglected the mean deviations become 0.051 Å and 0.040 Å, respectively, becoming reasonably accurate for the DFT methods used.

Beginning with the geometric parameters pertaining to the actinyl fragments, the exo-oxygen containing An=O1 actinyl bond is found to range in length, over 15 hexavalent complexes, from 1.783 to 1.808 Å, and over 15 pentavalent complexes, from 1.807 to 1.842 Å, representing relatively small changes in these bonds, across both series of oxidation states (Tables 2 and 4). The introduction of the TM to the secondary cavity can thus be said to have very little influence on the length of the An=O1 bond. Correspondingly, the very consistent An=O1 bond orders of 2.40 ± 0.02 support this (Tables 3 and 5). With the other actinyl bond An=O2 containing the endo-oxygen, a consistently longer bond length, over that of An=O1, is observed either because of O2 hydrogen bonding interactions for the six non-TM $[An^{VI}O_2(\mathbf{1})H_2L]$ and $[An^{V}O_2(\mathbf{1})H_2L]^-$ complexes, or to an even larger degree, because of the M−O2 TM bonding in the 24 $[An^{VI}O_2(\mathbf{2\text{-}5})L]$ and $[An^{V}O_2(\mathbf{2\text{-}5})L]^-$ TM containing structures. The lengthening of the An=O2 bond within these complexes can be interpreted as a desymmetrization of the typically symmetric linear actinyl fragment or in turn as a weakening of the An=O2 actinyl bond. A reduction in bond orders occurs for the hydrogen bonded O2, $[An^{VI}O_2(\mathbf{1})H_2L]$ and $[An^{V}O_2(\mathbf{1})H_2L]^-$ species, averaging 2.18 ± 0.03 and 2.02 ± 0.03, respectively (Table 3). The bond order decreases

Table 5. Gas-Phase Mayer Bond Orders[63,70] for $[An^{VI}O_2(\mathbf{2}\text{-}\mathbf{5})L]$ and $[An^{V}O_2(\mathbf{2}\text{-}\mathbf{5})L]^-$ Complexes[a]

complex	An=O1	An=O2	An−O3	An−N1,4[b]	An−N2,3	An−M	M−O2	M−O4	M−N5	M−N6,7	MN8
$[U^{VI}O_2(\mathbf{2})L]$	2.41	1.97	0.38	0.44(0)	0.56(1)	0.19	0.36	0.29	0.29	0.52(0)	0.20
$[U^{V}O_2(\mathbf{2})L]^-$	2.42	1.74	0.30	0.33(1)	0.47(0)	0.16	0.56	0.23	0.21	0.49(0)	0.18
$[Np^{VI}O_2(\mathbf{2})L]$[c]	2.41	1.80	0.33	0.39(1)	0.52(1)	0.38	0.54	0.29	0.38	0.54(0)	0.16
$[Np^{V}O_2(\mathbf{2})L]^-$	2.40	1.76	0.28	0.32(1)	0.46(0)	0.16	0.54	0.24	0.23	0.49(0)	0.19
$[Pu^{VI}O_2(\mathbf{2})L]$[c]	2.40	1.47	0.30	0.35(1)	0.49(1)	0.18	0.79	0.33	0.46	0.61(1)	0.10
$[Pu^{V}O_2(\mathbf{2})L]^-$	2.38	1.74	0.28	0.32(0)	0.45(0)	0.18	0.54	0.24	0.24	0.50(0)	0.20
$[U^{VI}O_2(\mathbf{3})L]$	2.42	1.83	0.37	0.42(1)	0.55(0)	0.50	0.48	0.32	0.25	0.59(1)	0.20
$[U^{V}O_2(\mathbf{3})L]^-$[d]	2.41	1.59	0.30	0.35(0)	0.49(0)	0.18	0.69	none	0.16	0.58(0)	0.15
$[Np^{VI}O_2(\mathbf{3})L]$	2.41	1.82	0.36	0.42(0)	0.54(0)	0.52	0.48	0.33	0.27	0.60(0)	0.20
$[Np^{V}O_2(\mathbf{3})L]^-$[d]	2.41	1.60	0.30	0.34(1)	0.47(1)	0.18	0.68	none	0.18	0.58(0)	0.15
$[Pu^{VI}O_2(\mathbf{3})L]$[c]	2.40	1.44	0.29	0.36(1)	0.49(1)	0.18	0.81	0.33	0.46	0.65(1)	0.33
$[Pu^{V}O_2(\mathbf{3})L]^-$[d]	2.39	1.59	0.29	0.33(0)	0.46(0)	0.20	0.68	none	0.19	0.58(0)	0.16
$[U^{VI}O_2(\mathbf{4})L]$	2.42	1.95	0.39	0.45(0)	0.56(0)	0.14	0.39	0.34	0.21	0.59(0)	0.17
$[U^{V}O_2(\mathbf{4})L]^-$	2.42	1.72	0.30	0.33(1)	0.47(0)	0.16	0.60	0.29	0.16	0.56(0)	0.14
$[Np^{VI}O_2(\mathbf{4})L]$	2.40	1.93	0.38	0.44(0)	0.54(0)	0.15	0.40	0.34	0.22	0.58(1)	0.17
$[Np^{V}O_2(\mathbf{4})L]^-$	2.41	1.74	0.28	0.32(0)	0.46(0)	0.16	0.57	0.30	0.17	0.56(0)	0.15
$[Pu^{VI}O_2(\mathbf{4})L]$	2.38	1.88	0.34	0.42(1)	0.47(1)	0.17	0.43	0.34	0.22	0.58(0)	0.16
$[Pu^{V}O_2(\mathbf{4})L]^-$	2.38	1.73	0.28	0.32(0)	0.45(0)	0.17	0.56	0.30	0.18	0.56(0)	0.16
$[U^{VI}O_2(\mathbf{5})L]$	2.42	1.95	0.39	0.46(1)	0.57(0)	0.10	0.38	0.29	0.14	0.57(1)	0.12
$[U^{V}O_2(\mathbf{5})L]^-$[d]	2.42	1.64	0.30	0.35(0)	0.49(0)	0.14	0.64	none	0.09	0.58(0)	0.09
$[Np^{VI}O_2(\mathbf{5})L]$	2.41	1.94	0.38	0.44(0)	0.55(0)	0.10	0.38	0.29	0.15	0.56(0)	0.12
$[Np^{V}O_2(\mathbf{5})L]^-$[d]	2.42	1.65	0.29	0.33(0)	0.47(0)	0.14	0.62	none	0.10	0.58(0)	0.09
$[Pu^{VI}O_2(\mathbf{5})L]$	2.39	1.89	0.34	0.42(0)	0.48(0)	0.11	0.40	0.29	0.15	0.56(1)	0.12
$[Pu^{V}O_2(\mathbf{5})L]^-$	2.39	1.75	0.28	0.32(0)	0.45(0)	0.13	0.53	0.22	0.12	0.54(0)	0.11

[a] O1 exo, O2 endo, O3 An THF, O4 M THF, M = Mn **2**, Fe **3**, Co **4**, Zn **5**. [b] Brackets contain maximum deviation from average. [c] Case 2 (3 short M−N bonds). [d] Case 3 (no M−O4 bond).

further (to less than full double bond) for the TM bonded O2, $[An^{VI}O_2(\mathbf{2}\text{-}\mathbf{5})L]$ and $[An^{V}O_2(\mathbf{2}\text{-}\mathbf{5})L]^-$ complexes, ranging from 1.97 to 1.44 and 1.76 to 1.59 for each species (Table 5). These changes in the actinyl bond can be considered as proof of the presence of a substantial M−O2 interaction.

Continuing with the actinyls, we see that in transitioning from the hexavalent to pentavalent oxidation states bond length increases are due to the reduced charge on the actinide metal. Average increases in An=O1 bond lengths of about 0.030 Å are observed, with the exception of $[Pu^{VI}O_2(\mathbf{2})L]$/$[Pu^{V}O_2(\mathbf{2})L]^-$ with only slight increases of 0.007 and 0.004 Å. Corresponding small increases in bond orders of 0.27 and 0.16 are also seen for these two Pu transitions in comparison to decreases seen for all other actinyl transitions.

As for the Hirshfeld atomic charges on these two plutonium metal complexes they are found to increase by 0.04 and 0.02 e with increased valency compared to an average increase for the other valency transitions of 0.08 ± 0.03 e (Tables S1 and S2, Supporting Information).

Taking a closer look at the actinyl fragment charges we find that the $An^{VI}O_2$ fragments have charges of nearly 0 e with the exception of $[Pu^{VI}O_2(\mathbf{2},\mathbf{3},\mathbf{5})L]$ with −0.15, −0.12, and −0.10 e, respectively. This is not the case for the $An^{V}O_2$ fragments, however, which are found to have fragment charges of between −0.17 and −0.28 e with only one exception for $[Np^{V}O_2(\mathbf{3})L]^-$ with charge of −0.08 e. In comparison to the formal charges of the actinyl fragments (+2 and +1, respectively), one can see that substantial charge transfer from the equatorial ligands has taken place. This charge transfer suggests that a much larger degree of covalent bonding may be involved, between the actinyl units and the macrocyclic ligand, than that of the ionic model on which these structures were initially based.

Although the actinides are found to be nearly planar within the N_4 cavity, the TMs are typically located slightly above the N_4 cavity plane (0.155 Å in the case of $[U^{VI}O_2(\mathbf{3})L]$ for example). For the most part consistency is seen for the bond lengths of the pair of cavity pyrrolic nitrogens. The pyrrolic An−N2,3 and M−N6,7 bonds are on average significantly stronger and shorter than their neutral Schiff-base counterparts with An−N1,4 and M−N5,8 bond lengths and distances. The actinide complexes with lower oxidation states show a noticeable increase in bond lengths for the pyrrolic nitrogens moving closer to the cavity center (equidistant and planar to all four nitrogens) leading to a reduction in Schiff-base nitrogen bond distances. For the M−N5 and M−N8 distances of the Schiff-base nitrogens we see significant variations in length—from being nearly equal in length for $[Np^{V}O_2(\mathbf{3})L]^-$ to having a difference of 1.164 Å for $[Pu^{VI}O_2(\mathbf{2})L]$.

An offset of the TM from the center of the cavity manifests itself in the difference in TM to Schiff-base nitrogen bond distances and is found to occur to varying degrees for most TM containing structures. As for the atomic charges on the eight nitrogens of the macrocyclic ligand they are almost always found to be −0.10 ± 0.02 e with the exception of the N6,7 pyrrolic nitrogens of $[Pu^{VI}O_2(\mathbf{3})L]$ which are −0.06 ± 0.01 e and the N6,7 pyrrolic nitrogens of the vacant cavity for the $[An^{VI}O_2(\mathbf{1})H_2L]$ complexes which are all −0.02 e.

Bonding of the THF solvent molecules to the actinide metals is considered to be part of the first solvation shell for case 1 structures, and as such the actinide coordination is considered to be a slightly distorted pentagonal bipyramid. An−O3 bond distances range from 2.468 to 2.649 Å, with the shortest bond distances seen in the $[An^{VI}O_2(\mathbf{1})H_2L]$ complexes. As for the TM to THF bond distances, M−O4 = 2.150 to 2.466 Å, they are found to be always shorter than that of the An−O3 bond distances, consistent with the difference in size between the 3d TM and the An atom. Comparatively, very little variation is seen for TM complexes

with first solvation shell THF coordination to the TM, cases 1 and 2, where bond orders average 0.33 ± 0.08 for An−O3 and 0.29 ± 0.07 for M−O4. The atomic charges on either of the THF oxygens are consistently found to be −0.06 ± 0.01 e.

For case 2 structures, [$Np^{VI}O_2$(**2**)L], [$Pu^{VI}O_2$(**2**)L], and [$Pu^{VI}O_2$(**3**)L], all three instances have TMs significantly more offset from the center of the cavity. In this case, the TM is found to have three strong cavity bonds to nitrogen, instead of two. A key feature of these structures is the shortening of the TM to Schiff-base nitrogen bond M−N5, to bond lengths of 2.293, 2.133, and 2.111 Å. Corresponding bond orders are 0.38, 0.46, and 0.46. For these structures there is a noticeable loss of symmetry in the TM cavity and substantial distortion can be seen to occur, for example, see the comparison between side and front views of [$Pu^{V}O_2$(**2**)L]$^-$ (top) and [$Pu^{VI}O_2$(**2**)L] (bottom) (Figure 2). The differences between the M−N5 and M−N8 bond distances are 0.756, 1.164, and 1.101 Å, respectively, compared to 0.231 Å or less for the remaining TM complexes. These differences can be regarded as a rough indication of the degree to which the metal is offset from center. However, the offset appears to be an inherent feature of these structures as seen from the differences of the two experimental examples tabulated, 0.310 Å for [$U^{VI}O_2$(**2**)L] and 0.557 Å for [$U^{VI}O_2$(**4**)L] (Table 2). Alternatively, further analysis of these structures without the weakly bound THF solvent molecule attached to the TM, should be checked to verify which structure has the lowest Gibbs free energy.

Another feature of the case 2 structures is the change in the cofacial angle (formed between the two nearly planar cavities). The cofacial angle is taken as an average of two angles N2−X1−N7 and N3−X2−N6, where X1 and X2 represent dummy atoms placed at the center of each aryl ring. The average cofacial angle for the structures without TMs [$An^{VI}O_2$(**1**)H_2L]/[$An^{V}O_2$(**1**)H_2L]$^-$ is 56.5 ± 0.5°, while progressively decreasing with An^{VI}/An^{V} valency by 0.7, 0.5, and 0.2° across the actinyl series. With the addition of TMs larger cofacial angles are seen averaging 58.8° and 62.0° for An^{VI} and An^{V} complexes. However, some variation is seen for TM containing complexes for both the $An^{VI/V}$ oxidation states, with Fe complexes having the largest average cofacial angles of 58.6/63.9°. The largest variation between actinyl oxidation states is seen for [$Pu^{V}O_2$(**2**)L]$^-$ with 62.3 ± 0.1° compared to that of [$Pu^{VI}O_2$(**2**)L] with 56.3 ± 4.3° (Table 1).

As for the case 3 structures, [$U^{V}O_2$(**3**)L]$^-$, [$Np^{V}O_2$(**3**)L]$^-$, [$Pu^{V}O_2$(**3**)L]$^-$, [$U^{V}O_2$(**5**)L]$^-$, and [$Np^{V}O_2$(**5**)L]$^-$, with no THF−TM bond, the TMs are found to be pulled out of the cavity toward the actinyl-endo-oxygen. For example, Fe of [$U^{V}O_2$(**3**)L]$^-$ is 0.674 Å above the N_4 cavity plane compared to 0.155 Å for [$U^{VI}O_2$(**3**)L].

Evidence of M−O2 bond formation, for all 24 TM containing complexes, of 0.36 to 0.81 for bond orders (Table 5) and 2.066 to 1.821 Å for corresponding bond lengths is observed (Table 4). In looking at Figure 4 we see that Zn^{II} has the least and Mn^{II} the most variation in M−O2 bond length across the An^{VI} series. As well, Fe is the most strongly

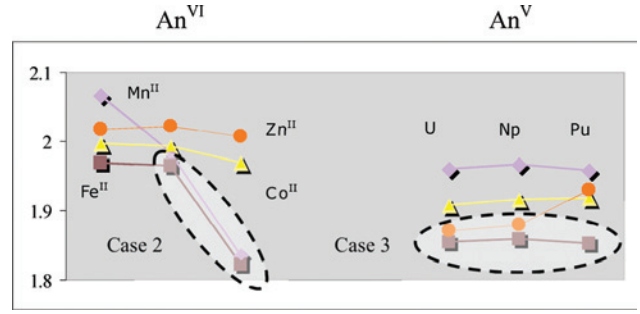

Figure 4. Variation in M−O2 bond lengths across An^{VI} and An^{V} series with fixed TM.

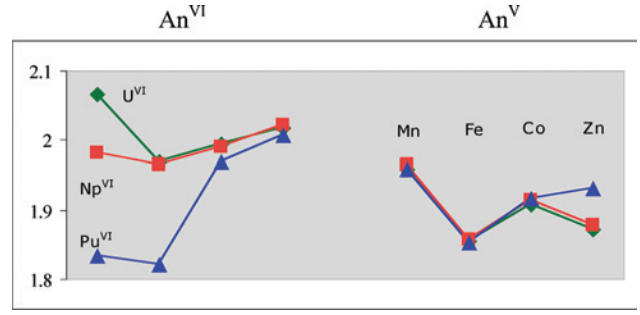

Figure 5. Variation in M−O2 bond lengths across TM series with fixed An^{VI} and An^{V}.

bound TM to O2 for all TM complexes. Also, the trend across the An^{V} series of TMs is seen to be nearly constant (with the one exception being [$Pu^{V}O_2$(**5**)L]$^-$). Furthermore, since the eight case 2 and case 3 structures are all seen to have the shortest bond lengths within there respective actinide oxidation types, we can say that the structural variation appears to correlate with the shortness of the M−O2 bond lengths.

As for Figure 5, we see that Np^{VI} has the least and Pu^{VI} the most variation in M−O2 bond length across the TM series. Here, we see that O2 of Pu^{VI} complexes is most strongly bound to all the TMs. Furthermore, we see decreasing bond length trends of Mn > Zn > Co > Fe for U^{V}, and Zn > Co > Mn > Fe for Np^{V} and Pu^{V}.

The An−O2−M bond angle is seen to remain fairly rigid for the majority of the structures with the lowest angle 141.3° occurring for the [$Pu^{VI}O_2$(**3**)L]$^-$ complex and the largest angle 161.6° occurring for the highly distorted [$Pu^{VI}O_2$(**2**)L] relative to the average of 144.9° for the six case 1 complexes containing Mn and Fe. However, both the Co and Zn TM complexes have larger An−O2−M average bond angles at 149.0° and 154.8°, respectively, for the case 1 complexes (Table 1).

Atomic charge averages for the [$An^{VI}O_2$(**2-5**)L] and [$An^{V}O_2$(**2-5**)L]$^-$ complexes are 0.29 e for Mn, 0.27 e for Fe, 0.21 e for Co, and 0.40 e for Zn. The atomic charges, found on Mn, Fe, and Zn, are found to be consistently higher than those on Co. As such, with the case 2 and 3 structural variations identified in the TM complexes found to occur with Mn, Fe, and Zn and not with Co, a likely contributing factor is the larger atomic charge found on these three TMs (Table S2, Supporting Information).

Table 6. Gas-Phase Energies (p5) and Oxidation Reduction Potentials (p5 and ADF) for $[An^{VI}O_2(\mathbf{1})H_2L]/[An^{V}O_2(\mathbf{1})H_2L]^-$ Couples (eV)

Redox half-reactions	ΔE_{298}	ΔG_{298}	ΔG_{solv}	vs Fc^+/Fc^a	$+Hay^b_{corr}$
$[U^{VI}O_2(\mathbf{1})H_2L] + e^- \rightarrow [U^{VI}O_2(\mathbf{1})H_2L]^-$	−1.72	−1.85	−3.29	−1.98	−1.67
$[Np^{VI}O_2(\mathbf{1})H_2L] + e^- \rightarrow [Np^{VI}O_2(\mathbf{1})H_2L]^-$	−2.39	−2.47	−4.07	−1.19	−0.02
$[Pu^{VI}O_2(\mathbf{1})H_2L] + e^- \rightarrow [Pu^{VI}O_2(\mathbf{1})H_2L]^-$	−2.74	−2.80	−4.59	−0.68	−0.47

[a] ΔG_{solv} of Fc^+/Fc redox couple = −5.27 eV. [b] Hay correction U, Np, and Pu = −0.31, −1.17, and −0.21 eV.

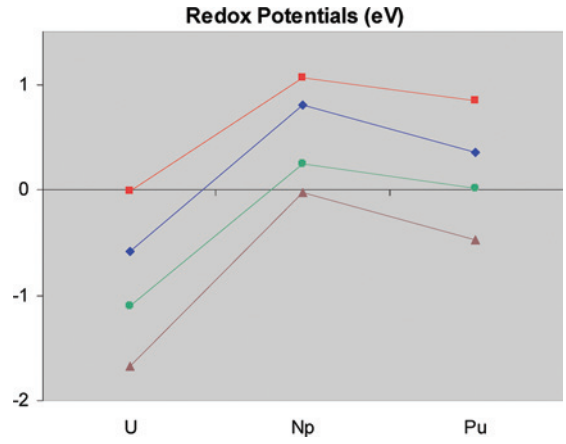

Figure 6. Redox potentials across actinide series for both the $[An^{VI}O_2(\mathbf{1})H_2L]/[An^{V}O_2(\mathbf{1})H_2L]^-$ couple relative to the ferrocene/ferrocenium couple (calculated, brown up triangles; predicted, green circles) and the $AnO_2(H_2O)_5^{2+/1+}$ couple relative to the standard hydrogen couple (calculated, blue diamonds; experiment, red squares), see the text (eV).

Measurement of the metal-to-metal An−M distances was obtained with the intent of determining the proximity that the two metals have to each other within the TM complexes (Table 4). The bond orders for three structures, 0.38 for $[Np^{VI}O_2(\mathbf{2})L]$, 0.50 for $[U^{VI}O_2(\mathbf{3})L]$, and 0.52 for $[Np^{VI}O_2(\mathbf{3})L]$ are indicative of a significant amount of charge built up between the two metals suggesting the possibility of bond formation. Comparatively, An−M bond orders of only 0.17 ± 0.03 are seen for all other TM complexes, which can be interpreted as no bond formation. With the corresponding actinide to TM bond distances of 3.712, 3.679, and 3.670 Å it is thought that these bond orders are an artifact of the calculation method and that no bonds exist between the An and TMs. This does, however, bring into question whether the other bond orders obtained can be trusted, and based on comparison to bond lengths that have be measured against experiment they seem reasonable.

B. Oxidation and Reduction Potentials. For the ferrocenium/ferrocene (Fc^+/Fc) half-reaction (reaction 2) we obtained a gas-phase reduction potential of −5.27 eV. Calculated values for the $[An^{VI}O_2(\mathbf{1})H_2L]/[An^{V}O_2(\mathbf{1})H_2L]^-$ series of redox potentials were −1.67, −0.02, and −0.47 eV (U, Np, and Pu) relative to the Fc^+/Fc couple after taking into account the corresponding Hay corrections[52] (Table 6).

A recent study of penta-aqua actinyls yielded p5 PBE/DZP reduction potentials for the series of complexes containing uranium, neptunium, and plutonium of −0.58, 0.80, and 0.36 eV relative to a Fc^+/Fc potential of −5.20 eV.[43,44,52] Comparing the redox couple results of the $[AnO_2(H_2O)_5]^{2+/1+}$ series to those of the $[An^{VI}O_2(\mathbf{1})H_2L]/[An^{V}O_2(\mathbf{1})H_2L]^-$ series of this study, we find the same $Np^{VI/V} > Pu^{VI/V} > U^{VI/V}$ trend (Figure 6).

Furthermore with available experimental results for the $[AnO_2(H_2O)_5]^{2+/1+}$ series relative to the Fc^+/Fc redox couples being −0.01, 1.07, and 0.84 eV,[43,52] we were able to determine the corresponding amounts (0.57, 0.27, and 0.48 eV) by which the calculated results underestimated these experimental values. Using these underestimated values as corrections we obtained rough approximations (−1.10, 0.25, and 0.01 eV) to experimental values for the $[An^{VI}O_2(\mathbf{1})H_2L]/[An^{V}O_2(\mathbf{1})H_2L]^-$ redox potentials across the series (Figure 6, green circles). Comparing the newly predicted redox potential to the available cyclic voltammetry data for the $[U^{VI}O_2(\mathbf{1})H_2L]/[U^{V}O_2(\mathbf{1})H_2L]^-$ redox couple of −1.18 eV, obtained in a $THF/NBu^n_4BF_4$ solvent,[69] we find it to be within 0.08 eV of our predicted value.

While the empirical correction as applied above is quite successful, we note that the systematic underestimation of the calculated redox potentials may be due to the use of approximate DFT as has been discussed in the literature.[66,67] (See the discussion in the "Methods" section above.) It would be most satisfying, of course, to further test this hypothesis by applying a method such as CASPT2 to the current systems; however, this is entirely unfeasible because of the number of atoms and electrons involved.

Conclusion

In this paper density functional computational methods are used to study a new form of binucleating Schiff-base macrocycles containing actinyl cations $U^{VI}O_2^{2+}$, $U^{V}O_2^{+}$, $Np^{VI}O_2^{2+}$, $Np^{V}O_2^{+}$, $Pu^{VI}O_2^{2+}$, and $Pu^{V}O_2^{+}$ within the first cavity and 3d TM cations Mn^{II}, Fe^{II}, Co^{II}, and Zn^{II} within the second cavity.

Formal bond order evidence is provided for TM to actinyl-endo-oxygen partial bond formation for all $[An^{VI}O_2(\mathbf{2\text{-}5})L]$ and $[An^{V}O_2(\mathbf{2\text{-}5})L]^-$ complexes (M−O2 = 0.36 to 0.81). Bond order evidence of metal-to-metal partial bond formation found for: $[U^{VI}O_2(\mathbf{3})L]$ (0.50), $[Np^{VI}O_2(\mathbf{2})L]$ (0.38), and $[Np^{VI}O_2(\mathbf{3})L]$ (0.52) is thought to be an artifact of the theoretical formal bond order calculations, since all have actinide to TM bond distances of greater than 3.670 Å.

Three instances of case 2 are identified, where offset TMs form 3 rather than 2 strong N bonds resulting in distorted geometries for $[Np^{VI}O_2(\mathbf{2})L]$, $[Pu^{VI}O_2(\mathbf{2})L]$, and $[Pu^{VI}O_2(\mathbf{3})L]$. As well, five instances of case 3 occur, where TMs of the $[U^{V}O_2(\mathbf{3})L]^-$, $[Np^{V}O_2(\mathbf{3})L]^-$, $[Pu^{V}O_2(\mathbf{3})L]^-$, $[U^{V}O_2(\mathbf{5})L]^-$, and $[Np^{V}O_2(\mathbf{5})L]^-$ complexes are located above the cavity plane closer to actinyl-endo-oxygen displacing THF solvent molecules. Furthermore, since the eight case 2 and case 3 structures are all seen to have the shortest bond lengths within

(68) Tait, C. D. *Actinide Research Quarterly* **2004**, *1*, 20.
(69) Arnold, P. L.; Patel, D.; Love, J. B., unpublished results, 2007.
(70) Mayer, I. *Simple theorems, proofs, and derivations in quantum chemistry*; Kluwer Academic/Plenum Publishers: New York, 2003.

their respective actinide oxidation types, we can say that the structural variation correlates with the shortness of the M−O2 bond lengths.

Iron (Fe) was identified to be the most strongly bound TM to the actinyl-endo-oxygen O2 for all TM complexes, whereas, O2 of Pu^{VI} complexes is most strongly bound to all the TMs. Also, with most of the chemical variation found to occur in Mn, Fe and Zn complexes the most likely common denominator is thought to be the greater atomic charge found on Mn, Fe, and Zn relative to Co.

Redox potentials for $[An^{VI}O_2(\mathbf{1})H_2L]/[An^{V}O_2(\mathbf{1})H_2L]^-$ couples were determined to have a nearly identical trend $Np^{VI/V} > Pu^{VI/V} > U^{VI/V}$ to those previously studied for $[AnO_2(H_2O)_5]^{2+/1+}$,[43,52] where Np^{VI} is the most easily reduced to Np^{V}. Therefore, we can conclude that this trend in relative redox potentials is primarily a function of the actinide metal and not the ligand system. The Shamov et al.[43,44] results were found to underestimate the experimental $[AnO_2(H_2O)_5]^{2+/1+}$ redox potentials by 0.57 eV, 0.27 eV, and 0.48 eV for U, Np, and Pu, respectively. These energy displacements allowed us to roughly predict $[An^{VI}O_2(\mathbf{1})H_2L]/[An^{V}O_2(\mathbf{1})H_2L]^-$ redox potentials of U = −1.10 eV, Np = 0.25 eV, and Pu = 0.01 eV. We then compared the predicted value for the uranyl redox potential $[U^{VI}O_2(\mathbf{1})H_2L]/[U^{V}O_2(\mathbf{1})H_2L]^-$ of −1.10 eV to the experimental cyclic voltammetry redox potential result of −1.18 eV determined in a THF/$NBu^n_4BF_4$ solvent.[69] The 0.08 eV difference lends some support to the potential accuracy of the ad hoc values predicted for both the $[Np^{VI}O_2(\mathbf{1})H_2L]/[Np^{V}O_2(\mathbf{1})H_2L]^-$ and $[Pu^{VI}O_2(\mathbf{1})H_2L]/[Pu^{V}O_2(\mathbf{1})H_2L]^-$ redox potentials.

To summarize, computational methods are used to provide reasonably expedient and reasonably accurate results for bimetallic actinide-containing structures of this size (108 atoms) while at the same time taking into account relativistic effects in determining gas-phase geometries and gas- and solution-phase energetics.

Acknowledgment. J.J.B. and G.S. are grateful to Dr. D. N. Laikov, Moscow/Stockholm for making his Priroda code available. Financial support from the Natural Sciences and Engineering Research Council of Canada is gratefully acknowledged. Also, thanks to Dr. Gernot Frenking of University of Marburg for resolving an issue with the usage of the ADF ETS energy decomposition method and suggesting the use of NBO analysis instead.

P.L.A., D.P., and J.B.L. thank the University of Edinburgh, Actinet, and the Royal Society for funding.

Supporting Information Available: Tables S1 and S2 containing calculated Hirshfeld atomic charges[64] for the various complexes. This material is available free of charge via the Internet at http://pubs.acs.org.

IC8010772